Journal of Alloys and Compounds 857 (2020) 158230

Contents lists available at ScienceDirect

Journal of Alloys and Compounds

journal homepage: www.elsevier.com/locate/jalcom

Magnetic properties and ferrimagnetic structures of Mn self-doped perovskite solid solutions $(Ho_{1-x}Mn_x)MnO_3$

Andreas Dönni[a], Vladimir Y. Pomjakushin[b], Lei Zhang[a,c], Kazunari Yamaura[a,c], Alexei A. Belik[a,*]

[a] International Center for Materials Nanoarchitectonics (WPI-MANA), National Institute for Materials Science (NIMS), Namiki 1-1, Tsukuba, Ibaraki 305-0044, Japan
[b] Laboratory for Neutron Scattering and Imaging, Paul Scherrer Institute, 5232 Villigen PSI, Switzerland
[c] Graduate School of Chemical Sciences and Engineering, Hokkaido University, North 10 West 8, Kita-ku, Sapporo, Hokkaido 060-0810, Japan

ARTICLE INFO

Article history:
Received 18 October 2020
Received in revised form 24 November 2020
Accepted 5 December 2020
Available online 13 December 2020

Keywords:
$GdFeO_3$-type perovskites
Crystal structure
High-pressure synthesis
Neutron diffraction
Magnetic structure

ABSTRACT

A high-pressure synthesis method was employed to prepare $(Ho_{1-x}Mn_x)MnO_3$ solid solutions with x = 0.2 and 0.3 (at about 6 GPa and 1,670 K) and magnetic properties and structures were investigated by magnetic, dielectric and neutron diffraction measurements. Both samples crystallize in the $GdFeO_3$-type *Pnma* perovskite structure, and both samples show magnetization reversal behavior below the compensation temperature of about 35 K (at H = 100 Oe). The magnetization reversal phenomena are originated from a ferrimagnetic (FiM) structure which takes place below T_C = 76 K (x = 0.2) and 102 K (x = 0.3) and is built from ferromagnetic (FM) ordering of Mn^{3+} and Mn^{4+} cations at the B site which are antiferromagnetically (AFM) coupled with Ho^{3+} and Mn^{2+} cations at the A site. The magnetic moment of Ho^{3+} cations increases significantly with deceasing temperature, and it overcomes the saturated magnetic moment of Mn^{3+} and Mn^{4+} cations at the B site. Field-induced first-order transitions were found in both compounds below about 35 K. Neutron diffraction measurements on the x = 0.2 sample found a collinear FiM structure between 76 K and 40 K, and the development of spin canting at the A site below 40 K. The coexistence of Ho^{3+} and Mn^{2+} at the A-site gives rise to additional short-range magnetic ordering of Ho^{3+} and to strain effects along the a-direction which are stronger than in $(R_{1-x}Mn_x)MnO_3$ materials with heavier and smaller rare-earths cations.

1. Introduction

Magnetic phase transitions that take place in perovskite-structure oxides ABO_3 with A = rare-earth (R) elements and B = 3*d* transition metals have been attracting interest and attention for decades. This is because rich phenomena can be studied such as delicate balance and competitions between different magnetic anisotropies (single-ion anisotropy, Dzyaloshinskii-Moriya interactions, symmetric anisotropic exchange) [1], temperature-induced spin-reorientation (SR) transitions (e.g., in $RFeO_3$ and $RCrO_3$) [1], laser-pulse-induced SR transitions [2], temperature-induced magnetization reversal [3,4], spin-induced ferroelectricity (e.g., in $RMnO_3$) [1,5], spin-orbital couplings (in $RMnO_3$ and $RTiO_3$) [1], and spin-orbital entanglement (especially pronounced in RVO_3) [1,6].

Solid solutions on the A site allow fine tuning of structural and magnetic exchange parameters on the B site as in $R1_{1-x}R2_xMnO_3$ [7,8]. On the other hand, solid solutions on the B site introduce significant structural and exchange disorder and competitions of different exchange interactions [4] sometimes producing more complex phase diagrams than the initial end members, e.g., in the $RFe_{0.5}Cr_{0.5}O_3$ series [9]. Therefore, investigation of different solid solutions is a way to find new behaviors of perovskite-structure oxides. It was found that the introduction of magnetic Mn^{2+} cations into the A sites of $RMnO_3$ (R = Er-Lu) significantly modifies magnetic behaviors of $(R_{1-x}Mn_x)MnO_3$ solid solutions [10–12] in comparison with the parent $RMnO_3$ compounds [13–17] or $(R_{1-x}A_x)MnO_3$ solid solutions with A = Ca^{2+}, Sr^{2+}, or other non-magnetic cations [18–20]. In particular, ferrimagnetic (FiM) structures are stabilized in $(R_{1-x}Mn_x)MnO_3$ for $x \geq 0.2$ (R = Tm and Lu) [11,12], first-order SR transitions occur in $(Er_{1-x}Mn_x)MnO_3$ [10], and magnetization reversal phenomena take place in $(Tm_{1-x}Mn_x)MnO_3$ for $x \geq 0.2$ [12].

Magnetic properties of $(R_{1-x}Mn_x)MnO_3$ solid solutions with smaller R^{3+} cations could be independent of R^{3+} cations at higher

* Corresponding author.
E-mail address: Alexei.Belik@nims.go.jp (A.A. Belik).

https://doi.org/10.1016/j.jallcom.2020.158230
0925-8388/

temperatures, where the Mn-Mn interactions at the B sites are dominant. This is observed in parent $RMnO_3$ compounds, where the magnetic phase diagram and magnetic transition temperatures, corresponding to the Mn sublattice, are nearly the same for R = Ho-Lu [13]. However, at lower temperatures, both $RMnO_3$ and $(R_{1-x}Mn_x)MnO_3$ might show unique magnetic properties due to effects of rare-earth magnetism because of different single-ion anisotropies and maximum ordered moments of R^{3+} cations. Therefore, detailed studies should be performed for each R^{3+} cation.

This work is focused on detailed characterization of $(Ho_{1-x}Mn_x)MnO_3$ solid solutions with x = 0.2 and 0.3. Orthorhombic $HoMnO_3$ (*Pnma* symmetry) – a parent compound of this study – shows a transition to an incommensurate (IC) spin structure with the propagation vector $\mathbf{k} = (k_0, 0, 0)$ [k_0 = 0.41 at 41 K] at the Mn site below $T_{N1,Mn}$ = 41 K [21]. The propagation vector exhibits a strong temperature dependence and then locks into a commensurate structure (with k_0 = 1/2) below $T_{N2,Mn}$ = 26 K. Below $T_{N3,Ho}$ = 22 K, a small ordered moment appears on the Ho^{3+} cations, and this moment strongly increases below about 9 K. Specific heat of $HoMnO_3$ shows anomalies at all three temperatures (41, 26, and about 9 K), while dc magnetic susceptibilities show only antiferromagnetic (AFM)-like anomalies at 6 K [21]. $HoMnO_3$ shows purely AFM behavior and a metamagnetic transition from about 10 kOe at 2 K. Polarization properties of $HoMnO_3$ supported this picture of phase transitions [22]. Note that somewhat different behavior and properties of $HoMnO_3$ were reported in Refs. [23,24] reflecting probably effects of the oxygen content on its properties. We found that properties of $(Ho_{1-x}Mn_x)MnO_3$ solid solutions are drastically different from those of $HoMnO_3$ with the stabilization of a FiM ground state, a significant rise of magnetic transition temperatures, the appearance of pronounced magnetization reversal effects, and the appearance of field-induced first-order transitions.

2. Experimental

$(Ho_{1-x}Mn_x)MnO_3$ solid solutions were synthesized from stoichiometric mixtures of Mn_2O_3 and Ho_2O_3 (99.9%) with x = 0.2 and 0.3. The mixtures were placed in Pt capsules and treated at high pressure of 6 GPa and high temperature of about 1,670 K for 2 h (heating time to the synthesis temperature was 10 min) in a belt-type high-pressure apparatus. After the heat treatments, the samples were quenched to room temperature (RT), and the pressure was slowly released. All the samples obtained were black pellets (quite friable in some cases). Several batches of $(Ho_{0.8}Mn_{0.2})MnO_3$ (with the total weight of 2.524 g) were prepared for neutron diffraction. Single-phase Mn_2O_3 was prepared from commercial MnO_2 (99.99%) by heating in air at 923 K for 24 h.

X-ray powder diffraction (XRPD) data were collected at RT on a RIGAKU MiniFlex600 diffractometer using CuKα radiation (2θ range of 8–100°, a step width of 0.02°, and scan speed of 1°/min). Powder neutron diffraction measurements on $(Ho_{0.8}Mn_{0.2})MnO_3$ were conducted on the multidetector high resolution powder diffractometer HRPT [25] at the Swiss Spallation Neutron Source (SINQ), Paul Scherrer Institute (PSI), Switzerland. Measurements were performed at temperatures between 1.7 and 130 K and an incident neutron wavelength of 1.89 Å (2θ range of 3.55–164.50°, and a step width of 0.05°). The diffraction patterns were analyzed by the Rietveld method using the *FullProf Suite* [26]. Possible models for the magnetic structures were deducted based on a group theory analysis using the program *BasIreps* which is part of the *FullProf Suite* package of programs [26].

Magnetic measurements were performed on a SQUID magnetometer (Quantum Design, MPMS-XL-7T) between 2 K and 400 K in different applied magnetic fields from 1 Oe to 70 kOe using zero-field-cooled (ZFC), field-cooled on cooling (FCC), and field-cooled on warming (FCW) temperature scans (temperature was changed in a step-like mode). Isothermal magnetization measurements (M versus H) were performed between −70 and 70 kOe at T = 5 K. In the ZFC M versus H measurements, samples were cooled in zero magnetic field from 300 K, and measurements were performed from 70 kOe to −70 kOe and from −70 kOe to 70 kOe. In the FCC M versus H measurements, samples were cooled in a magnetic field of $+H$ from 300 K, and measurements were performed from $+H$ to $-H$ and from $-H$ to $+H$. AC susceptibility measurements were performed with a Quantum Design MPMS-1T instrument at different frequencies (f) and different applied oscillating magnetic fields (H_{ac}). Specific heat, C_p, at different magnetic fields between 0 Oe and 90 kOe was recorded between 2 K and 300 K on cooling and heating by a pulse relaxation method using a commercial calorimeter (Quantum Design PPMS). Dielectric properties were measured using a NOVOCONTROL Alpha-A High Performance Frequency Analyzer between 5 K and 300 K on cooling and heating in a frequency range of 100 Hz and 2 MHz and in applied magnetic fields between 0 Oe and 90 kOe.

3. Results and discussion

3.1. Structural properties of $(Ho_{1-x}Mn_x)MnO_3$

XRPD data showed that $(Ho_{0.8}Mn_{0.2})MnO_3$ was single-phase but exhibited strong anisotropic broadening of some reflections (Fig. S1). $(Ho_{0.7}Mn_{0.3})MnO_3$ contained about 8 wt% of $HoMn_3O_6$-type impurity [27] and showed sharp reflections and nearly uniformed full-width-at-half-maximum. The appearance of the $HoMn_3O_6$-type impurity - a next perovskite phase in the quasi-binary Ho_2O_3-Mn_2O_3 phase diagram - suggests that the solubility limit in the $(Ho_{1-x}Mn_x)MnO_3$ solid solutions is located slightly below x = 0.3 at the synthesis conditions used.

Neutron diffraction experiments were performed on the single-phase composition $(Ho_{0.8}Mn_{0.2})MnO_3$. The temperature dependence of the orthorhombic lattice parameters (a–c) and the unit cell volume (V) below T = 130 K is shown in Fig. 1. For cooling from the FiM phase transition at T_C = 76 K to 1.7 K, changes in the lattice parameters show a strong decrease for a ($\Delta a \approx -0.005$ Å), a strong increase for b ($\Delta b \approx +0.005$ Å), and a weak temperature dependence for c. Anomalies of a, b, c and V appear around 20 K, where a significant increase of the ordered Ho^{3+} moments is observed (see Section 3.2).

Experimental, calculated, and difference neutron diffraction patterns of $(Ho_{0.8}Mn_{0.2})MnO_3$ measured in the paramagnetic state at T = 130 K are shown in Fig. 2a. The Rietveld refinement of the expected crystal structure shown in Fig. S2 gives a poor agreement (χ^2 = 7.34) due to the presence of anisotropic line-shape broadening of some Bragg peaks. Strain broadening was modelled for (100) anisotropic broadening in an orthorhombic lattice using quartic form in reciprocal space [28,29]. Orthorhombic symmetry allows six independent anisotropic strain parameters S_{HKL} [29]. Three of them turned out to be large (in the order of decrease S_{400}, S_{202} and S_{220}) and were refined. The other three (S_{040}, S_{004} and S_{022}) were found to be small and set to zero. The refinement that includes corrections for strain broadening shown in Fig. 2a gives a much better agreement (χ^2 improved from 7.34 to 2.17). Obtained structural parameters for $(Ho_{0.8}Mn_{0.2})MnO_3$ at 130 K, strain parameters, bond lengths, Mn-O-Mn bond angles, and bond-valence sums (BVS) [30] are summarized in Tables 1 and 2. The presence of Ho^{3+} and Mn^{2+} (with different sizes and masses) at the A site causes strong microstrain effects along the a-direction. With the large contrast between the neutron scattering lengths b_{Ho} = 8.01 fm and b_{Mn} = − 3.73 fm, neutron data are sensitive to the occupation of Ho^{3+} and Mn^{2+} at the A site. Compared to the nominal composition of $(Ho_{0.8}Mn_{0.2})MnO_3$, the refinement gave a slightly higher occupation of Ho^{3+} (83%). Note that in the Rietveld refinement, the values of the strain parameters are correlated with the values for lattice constants, Debye-Waller factors and

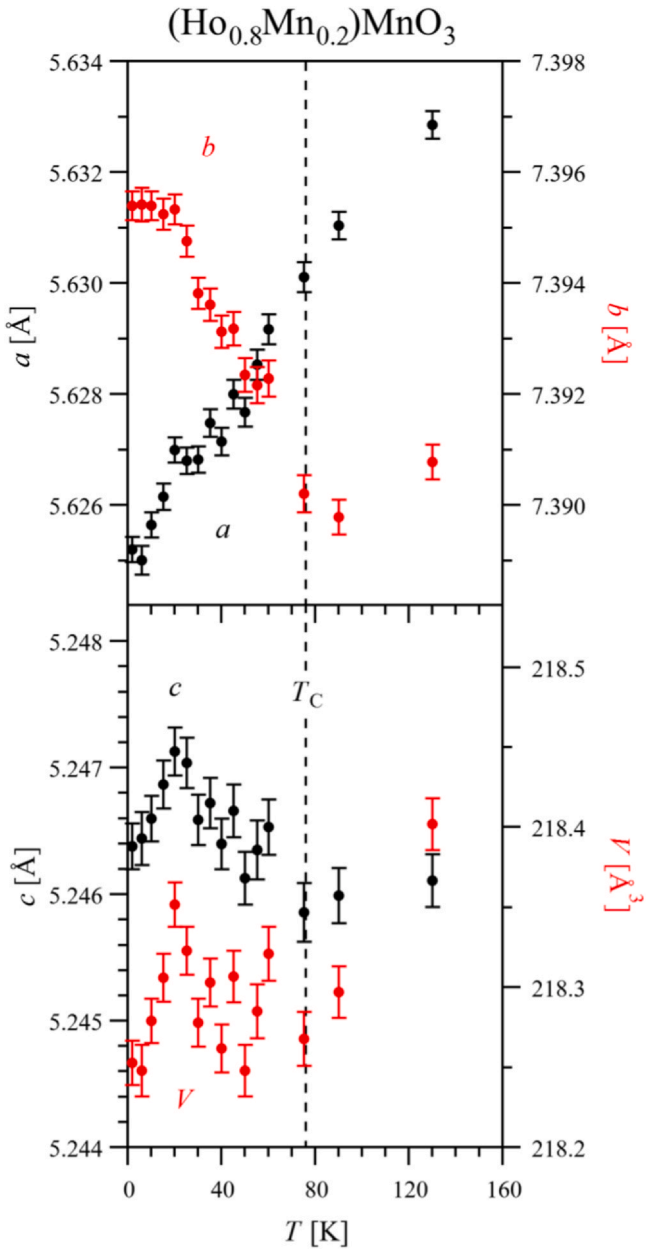

Fig. 1. Temperature dependence of the orthorhombic lattice parameters (a, b, and c) and the unit cell volume (V) in $(Ho_{0.8}Mn_{0.2})MnO_3$ refined from neutron diffraction data. The vertical dashed line indicates the FiM phase transition at T_C = 76 K.

also occupation factors. Strong strain corrections have a tendency to give slightly smaller values for lattice constants, smaller values for Debye-Waller factors and a slightly larger occupation factor for Ho^{3+}.

In the following we compare our results on $(Ho_{0.8}Mn_{0.2})MnO_3$ with the previously studied FiM materials $(Tm_{0.7}Mn_{0.3})MnO_3$ [12] and $(Lu_{0.6}Mn_{0.4})MnO_3$ [11]. The temperature dependence of the lattice constants below T_C shows a similar trend in $(Ho_{0.8}Mn_{0.2})MnO_3$ and $(Tm_{0.7}Mn_{0.3})MnO_3$, whereas the absence of rare-earth magnetism in $(Lu_{0.6}Mn_{0.4})MnO_3$ leads to a smaller and similar decrease for a and c ($\Delta a \approx \Delta c \approx -0.003$ Å). A common feature of all three FiM materials is a minimum of b near the FiM phase transition T_C. Strain effects strongly increase with the size of the rare-earth cation. In $(Ho_{0.8}Mn_{0.2})MnO_3$ (S_{400} = 8.1(2)), the largest strain parameter S_{400} is about twice as large as in $(Tm_{0.7}Mn_{0.3})MnO_3$ (S_{400} = 4.22(9)) and an order of magnitude larger than in $(Lu_{0.6}Mn_{0.4})MnO_3$ (S_{400} = 0.61(2)). In contrast, the solubility limit of $(R_{1-x}Mn_x)MnO_3$ solid solutions decreases with increasing size of the rare-earth cation (from x slightly above 0.4 for R = Lu [11], to x close to 0.33 for R = Tm [12] and to x slightly below 0.3 for R = Ho). The distortion parameter of MnO_6 octahedra, Δ(Mn), is correlated well with the amount of Jahn-Teller-inactive Mn^{4+} cations at the B sites. In units of 10^{-4}, the Δ(Mn) values reach nearly 50 in undoped $RMnO_3$ [11–13] and are then reduced to 30 in $(R_{0.9}Mn_{0.1})MnO_3$ [11,12], 18 in $(Ho_{0.8}Mn_{0.2})MnO_3$, about 10 in $(Tm_{0.7}Mn_{0.3})MnO_3$ [12] and $(R_{0.667}Mn_{0.333})MnO_3$ [10], and 3 in $(Lu_{0.6}Mn_{0.4})MnO_3$ [11].

3.2. Magnetic structures of $(Ho_{0.8}Mn_{0.2})MnO_3$

The neutron diffraction patterns of $(Ho_{0.8}Mn_{0.2})MnO_3$ measured at 40 K (Fig. 2b) and 1.7 K (Fig. 2c) contain strong magnetic Bragg peaks, which can all be indexed with a commensurate propagation vector $\mathbf{k}$ = (0, 0, 0). We employed group theory analysis in order to consider the possible magnetic structures in accordance with the magnetic propagation vector and the crystal structure of $(Ho_{0.8}Mn_{0.2})MnO_3$. A calculation by the program *BasIReps* [24] for $\mathbf{k}$ = (0, 0, 0) and space group *Pnma* gives eight irreducible representations (IR) with different symmetry (Table 3). For the Mn2 atoms at the B site, four of the eight IR allow magnetic order, whereas for the Ho/Mn1 atoms at the A site, there are eight IR with magnetic order.

$$\Gamma_{Mn2}(\text{B site}) = 3\Gamma_1 + 3\Gamma_3 + 3\Gamma_5 + 3\Gamma_7.$$

$$\Gamma_{Ho/Mn1}(\text{A site}) = \Gamma_1 + 2\Gamma_2 + 2\Gamma_3 + \Gamma_4 + \Gamma_5 + 2\Gamma_6 + 2\Gamma_7 + \Gamma_8.$$

The observed magnetic structures of $(Ho_{0.8}Mn_{0.2})MnO_3$ at 40 and 1.7 K are FiM and belong to the IR Γ_7, which allows ordered magnetic moments along all 3 directions (F_x, A_y, C_z) at the B site and within the ac-plane (f_x, 0, c_z) at the A site. The components F_x and f_x describe FM order along the a-axis. For such a structure, Bragg peaks of magnetic and crystal structures have the same extinction rules and appear at the same 2θ values. The other components (A_y, C_z and c_z) describe AFM order along the b- and c-axes. Here, the 2θ values of the Bragg peaks of magnetic and crystal structures are different.

First we performed a refinement of the average ordered moments at A and B sites (Fit #1). The refinement at 40 K shown in Fig. 2b gives collinear FiM order with average ordered moments of $F_{x,\,ave}$ = 2.20(2) μ_B at the B site and $f_{x,\,ave}$ = −2.02(2) μ_B at the A site. Agreement values of the refinement were χ^2 = 2.32, R_{wp} = 3.27, R_{exp} = 2.15, R_{Bragg} = 4.13, $R_{Magnetic}$ = 5.49. The FiM structure at 40 K is displayed in Fig. 3. All ordered moments are parallel or antiparallel to the a-axis with AFM coupling between B and A sites. The difference pattern 40–130 K shown in the inset of Fig. 2b contains only magnetic Bragg peaks. Magnetic intensity is observed at the Bragg peak positions of the crystal structure (indicated in blue color) and not at the additional Bragg peak positions allowed by the magnetic propagation vector (indicated in red color).

At 1.7 K, the non-zero intensity observed for the magnetic (1, 0, 0), (1, 1, 0), (1, 2, 0) and (0, 2, 1) reflections (indicated in red color in the inset of Fig. 2c) is direct experimental evidence for the presence of a *non-collinear* canted FiM structure. The refinement at 1.7 K shown in Fig. 2c gives average ordered moments of $F_{x,ave}$ = 2.33(2) μ_B at the B site and $f_{x,ave}$ = −4.94(2) μ_B and c_z = 2.23(2) μ_B at the A site. Agreement values of the refinement were χ^2 = 3.02, R_{wp} = 3.75, R_{exp} = 2.16, R_{Bragg} = 4.26, $R_{Magnetic}$ = 3.46. The magnetic structure at 1.7 K is displayed in Fig. 4. Ordered moments at the A site exhibit a spin canting within the ac-plane. Note that for magnetic structures within IR Γ_7, no intensity is allowed for the magnetic peaks (0, 1, 0) at 2θ = 14.65° and (0, 0, 1) at 2θ = 20.71°, which is in agreement with our experiment (see insets of Fig. 2b and c).

Fig. 5a shows the temperature dependence of FCC magnetic susceptibility χ measured in a very small magnetic field of H = 1 Oe.

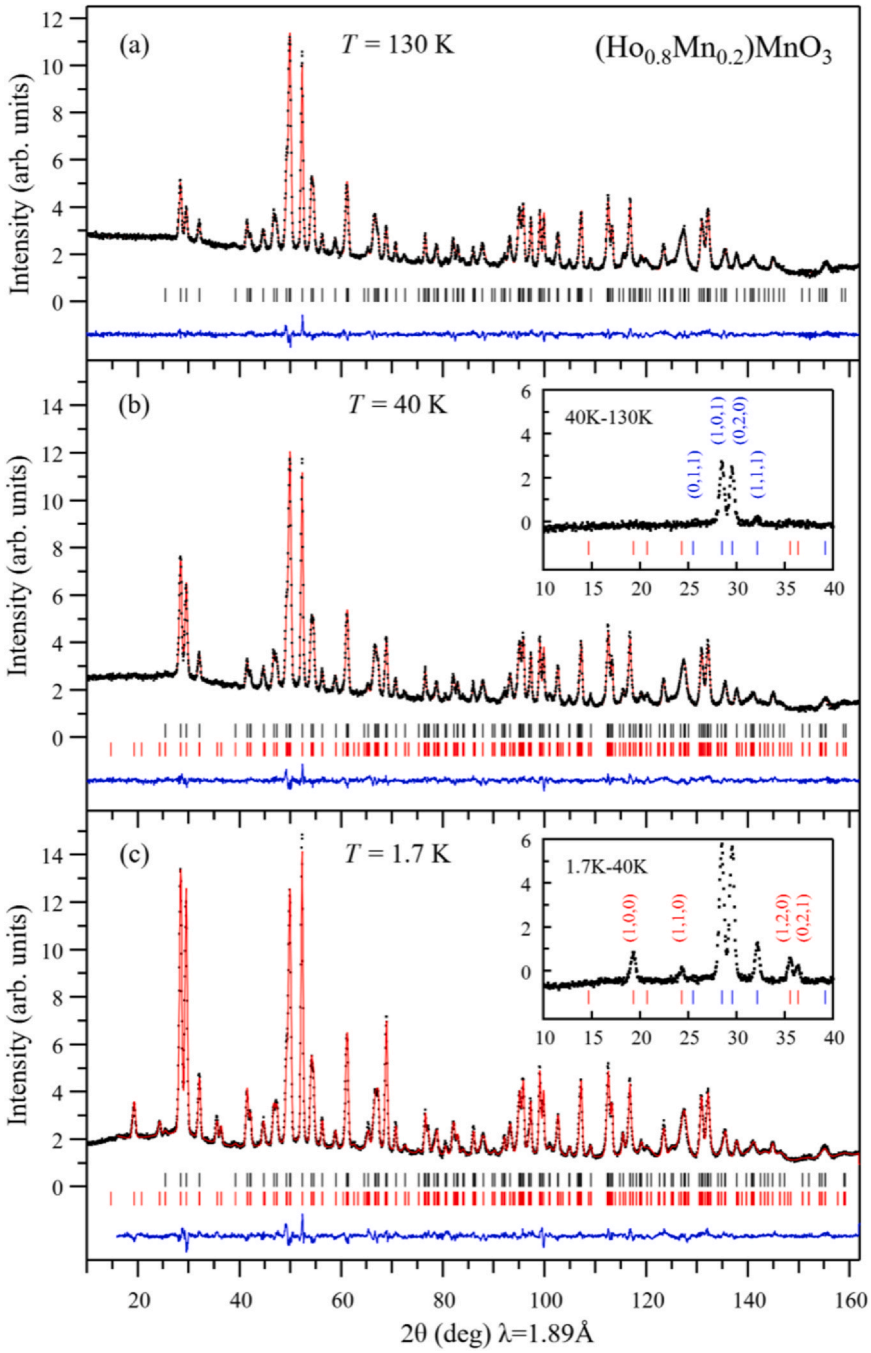

Fig. 2. Experimental (black dots), calculated (red line), and difference (blue line) neutron diffraction patterns of $(Ho_{0.8}Mn_{0.2})MnO_3$ in the paramagnetic state at $T = 130$ K (a) and in the magnetically ordered states at $T = 40$ K (b) and 1.7 K (c). The tick marks indicate Bragg peak positions of nuclear peaks (upper row, black) and magnetic peaks (lower row, red). The insets show parts of the difference patterns: 40–130 K and 1.7–40 K. (For interpretation of the references to colour in this figure legend, the reader is referred to the web version of this article.)

Around the FiM ordering temperature $T_C = 76$ K, χ increases from very small values to a small broad maximum near 60 K ($\chi = 12.3$ cm^3/mol) before crossing zero at the compensation temperature $T = 35$ K and decreasing towards a large negative value at 2 K ($\chi = -69.4$ cm^3/mol). The accuracy of the determination of the net macroscopic FM moment per formula unit ($F_{x,ave} + f_{x,ave}$) from our neutron diffraction data turned out to be good for the large values at low temperature, but rather poor for the smaller values close to zero at higher temperature. Therefore, as shown in Fig. 5a, we have decided to use the ($F_{x,ave} + f_{x,ave}$) values determined by neutron diffraction for the 3 lowest temperatures up to 10 K to adjust the scale to the FCC magnetic susceptibility data and performed the refinements at temperatures between 15 and 60 K with ($F_{x,ave} + f_{x,ave}$) fixed to the values of the magnetic susceptibility curve. The temperature dependence of the magnetic structure of $(Ho_{0.8}Mn_{0.2})MnO_3$ based on Fit #1 ($F_{x,ave}$, $f_{x,ave}$, $c_{z,ave}$) is displayed in Fig. 5b. The FM moment ($F_{x,ave} + f_{x,ave}$) reaches a large negative value of $-2.61(4)$ μ_B at 1.7 K compared to a much smaller positive maximum of 0.46(4) μ_B at 60 K. The determination of the AFM component ($c_{z,ave}$) is accurate and depends on the intensities of the magnetic (1, 0, 0), (1, 1, 0), (1, 2, 0) and (0, 2, 1) reflections (indicated in red color in the inset of Fig. 2c), which could be detected up to 35 K, but not at higher temperatures. With decreasing temperature, the FM ordered Mn2 moments at the B site ($F_{x,ave}$) monotonically increase below $T_C = 76$ K and reach the saturation value at around 20 K, at the same temperature below which an

Table 1
Values of crystal-structural parameters of paramagnetic $(Ho_{0.8}Mn_{0.2})MnO_3$ at 130 K derived from a Rietveld refinement of neutron diffraction data.

Atom	Site	g	x	y	z	B (Å^2)
Ho	4*c*	0.832(3)	0.0783(3)	0.25	0.9834(3)	0.21(5)
Mn1	4*c*	0.168(3)	= x(Ho)	0.25	= z(Ho)	= B(Ho)
Mn2	4*b*	1	0	0	0.5	0.22(5)
O1	4*c*	1	0.4619(4)	0.25	0.1059(3)	0.67(4)
O2	8*d*	1	0.3183(3)	0.0534(2)	0.6983(3)	0.79(3)

Space group *Pnma* (No 62), occupation factor (g). The lattice constants are a= 5.6329(3) Å, b= 7.3908(3) Å, c = 5.2461(2) Å, and the Volume is V=218.40(2) Å^3. Strain parameters [in units of 10^{-4}] are S_{400} = 8.1(2), S_{202} = 3.1(3), S_{220} = −1.17(7). Reliability indices of the refinement are χ^2 = 2.17, R_{wp} = 3.15%, R_{exp} = 2.14%, and R_{Bragg} = 4.06%.

Table 2
Selected bond lengths (Å), bond angles (deg), Bond Valence Sums, BVS, and Distortion parameters of MnO_6 (Δ(Mn)) for $(Ho_{0.8}Mn_{0.2})MnO_3$ at T = 130 K.

Ho/Mn1 – O1	2.252(2)
Ho/Mn1 – O1	2.254(3)
Ho/Mn1 – O2 (×2)	2.273(2)
Ho/Mn1 – O2 (×2)	2.485(2)
Ho/Mn1 – O2 (×2)	2.5763(16)
BVS(Ho^{3+})	3.11
BVS($Mn1^{2+}$)	1.66
Mn2 – O1 (×2)	1.9413(5)
Mn2 – O2 (×2)	1.9257(16)
Mn2 – O2 (×2)	2.1101(16)
BVS($Mn2^{3+}$)	3.28
Δ(Mn2)	17.6×10^{-4}
Mn2 – O1 – Mn2 (×2)	144.27(2)
Mn2 – O2 – Mn2 (×4)	144.94(7)

BVS = $\sum_{i=1}^{N} v_i$, $v_i = \exp[(R_0 - l_i)/B]$, N is the coordination number, B = 0.37, $R_0(Ho^{3+})$ = 2.023, $R_0(Mn^{2+})$ = 1.79, and $R_0(Mn^{3+})$ = 1.76 [30].
$\Delta = (1/N)\sum_{i=1}^{N}[(l_i - l_{av})/l_{av}]^2$, where $l_{av} = (1/N)\sum_{i=1}^{N} l_i$ is the average Mn-O distance and N is the coordination number.

accelerated growth is observed for the average ordered Ho/Mn1 moments at the A site ($-f_{x,\,ave}$, $c_{z,ave}$), consistent with an anomaly in the specific heat (C_p/T data also shown in Fig. 5b).

Apart from the difference of the magnetic form factors for Ho^{3+} and Mn^{2+} (not accurate), our neutron diffraction data cannot distinguish between the contributions from 80% of Ho^{3+} and 20% of Mn^{2+} to the average ordered moment at the A site ($-f_{x,ave}$, $c_{z,ave}$) and we had to use an approximation. For Fit #2 and Fit #3, we assigned the AFM component c_z to Ho^{3+} and correlated the ordered Mn moments at B and A sites as follows:

A site: $\mathrm{Mn}(f_{x,Mn},\ 0,\ 0)$, $\mathrm{Ho}(f_{x,Ho},\ 0,\ c_{z,Ho})$;

B site: $\mathrm{Mn}\,(F_{x,Mn},\ 0,\ 0)$;

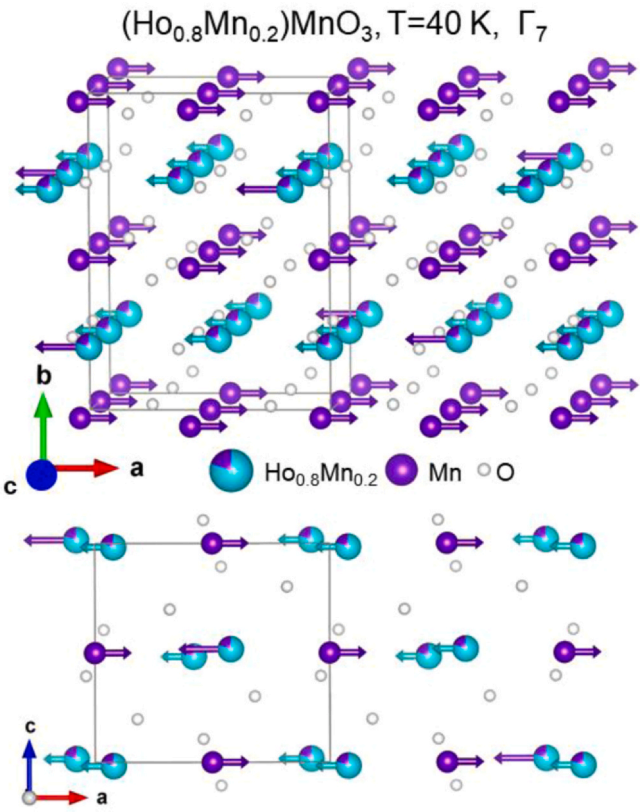

Fig. 3. Magnetic structure of $(Ho_{0.8}Mn_{0.2})MnO_3$ at T = 40 K refined from neutron diffraction data shown as a 3 dimensional illustration (top) and as a projection onto the *ac*-plane (bottom). Ordered magnetic moments (based on Fit #2) are shown by arrows in purple (Mn) and light blue (Ho). This drawing was made using the program VESTA [32]. (For interpretation of the references to colour in this figure legend, the reader is referred to the web version of this article.)

Constraint (Fit #2): $-f_{x,Mn} = 1.53 \cdot F_{x,Mn}$;

Constraint (Fit #3): $-f_{x,Mn} = 1.23 \cdot F_{x,Mn}$.

The constraint of Fit #2 is based on the experimentally observed ratio of the ordered Mn moments at B and A sites in $(Lu_{0.6}Mn_{0.4})MnO_3$ [11]. The constraint of Fit #3 has been used to refine the magnetic structure of $(Tm_{0.7}Mn_{0.3})MnO_3$ [12].

The resulting temperature dependence of the magnetic structure of $(Ho_{0.8}Mn_{0.2})MnO_3$ is shown in Fig. 5c (based on Fit #2) and in Fig. S3 (based on Fit #3). Both fits produce a similar qualitative behavior with identical values for the ordered Mn moments at the B site ($F_{x,Mn}$) and the AFM component at the A site ($c_{z,Ho}$). At low

Table 3
Magnetic arrangement allowed at the B site (4*b*) and A site (4*c*) for each of the irreducible representation (IR) based on group theory analysis (program *BasIreps* [26]) for space group *Pnma* and commensurate magnetic propagation vector **k** = (0, 0, 0).

IR	Site 4*b* (B site) Mn2	Site 4*c* (A site) Ho/Mn1	Magnetic space group [31]
Γ_1	(G_x, C_y, A_z)	$(-, c_y, -)$	Pnma (No. 62.1.502)
Γ_2		$(g_x, -, a_z)$	Pn'm'a' (No. 62.9.510
Γ_3	(C_x, G_y, F_z)	$(c_x, -, f_z)$	Pn'm'a (No. 62.6.507)
Γ_4		$(-, g_y, -)$	Pnma' (No. 62.5.506)
Γ_5	(A_x, F_y, G_z)	$(-, f_y, -)$	Pn'ma' (No. 62.8.509)
Γ_6		$(a_x, -, g_z)$	Pnm'a (No. 62.4.505)
Γ_7	(F_x, A_y, C_z)	$(f_x, -, c_z)$	Pnm'a' (No. 62.7.508)
Γ_8		$(-, a_y, -)$	Pn'ma (No. 62.3.504)
$F = m_1 + m_2 + m_3 + m_4$			$C = m_1 - m_2 + m_3 - m_4$
$G = m_1 - m_2 - m_3 + m_4$			$A = m_1 + m_2 - m_3 - m_4$

B site: $Mn2_1$ (0, 0, 1/2), $Mn2_2$ (1/2, 0, 0), $Mn2_3$ (0, 1/2, 1/2), $Mn2_4$ (1/2, 1/2, 0).
A site: Ho / $Mn1_1$ (x, 1/4, z), Ho / $Mn1_2$ (− x + 1/2, 3/4, z + 1/2), Ho / $Mn1_3$ (− x, 3/4, − z), Ho / $Mn1_4$ (x + 1/2, 1/4, − z + 1/2).

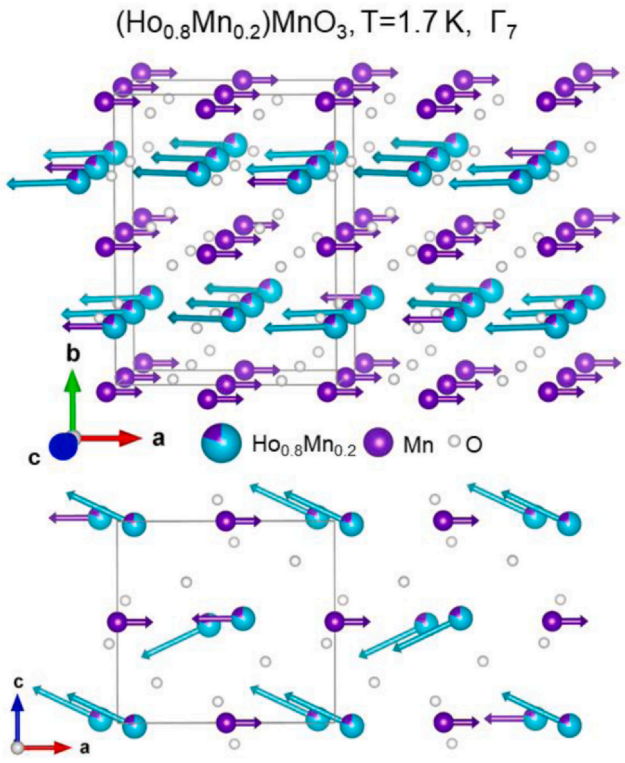

Fig. 4. Magnetic structure of $(Ho_{0.8}Mn_{0.2})MnO_3$ at $T = 1.7$ K refined from neutron diffraction data shown as a 3 dimensional illustration (top) and as a projection onto the *ac*-plane (bottom). Ordered magnetic moments (based on Fit #2) are shown by arrows in purple (Mn) and light blue (Ho). This drawing was made using the program VESTA [32]. (For interpretation of the references to colour in this figure legend, the reader is referred to the web version of this article.)

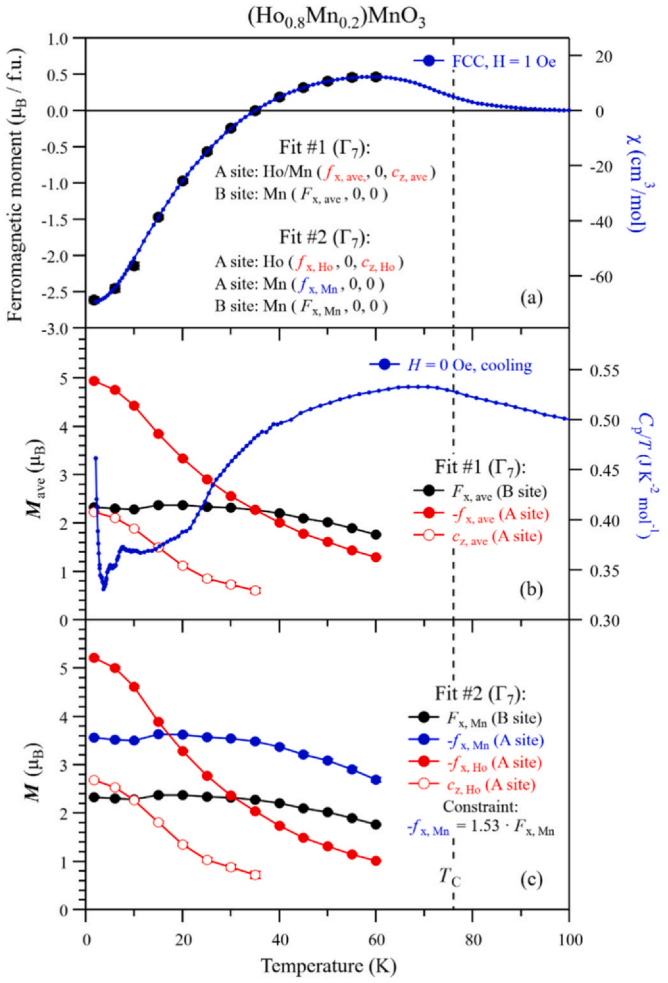

Fig. 5. Temperature dependence of the FiM structure of $(Ho_{0.8}Mn_{0.2})MnO_3$ refined from neutron diffraction data. Left-hand axes show the macroscopic FM moment per formula unit and the ordered magnetic Ho and Mn moments at A and B sites; right-hand axes display the magnetic susceptibility χ (FCC, $H = 1$ Oe) and the specific heat C_p/T. The vertical dashed line indicates the FiM phase transition at $T_C = 76$ K.

temperature the FM component at the A site is dominated by a large moment from the 80% of Ho^{3+} with only a small quantitative difference between $f_{x,Ho} = -5.22(3)$ μ_B (Fit #2) and $f_{x,Ho} = -5.36(3)$ μ_B (Fit #3). Therefore, without knowing the accurate value of the scale factor used in the constraint, we can consider that the magnetic structure of $(Ho_{0.8}Mn_{0.2})MnO_3$ is described well enough by Fit #2 (temperature dependence shown in Fig. 5c, magnetic structures illustrated in Figs. 3 and 4). The total ordered moments at 1.7 K are 5.87(3) μ_B for Ho^{3+}, 3.57(2) μ_B for Mn1 and 2.33(2) μ_B for Mn2.

Fig. 6 shows difference neutron diffraction patterns (with data measured at $T = 130$ K subtracted) around the magnetic Bragg peaks (1, 0, 1) and (0, 2, 0) measured at temperatures close to the FiM phase transition at $T_C = 76$ K. Broad diffuse magnetic scattering around the Bragg peak positions appears between 90 and 130 K and remains at lower temperature. On top of the diffuse scattering the magnetic Bragg peaks appear close to 75 K and gain intensity with decreasing temperature. Magnetic scattering in $(Ho_{0.8}Mn_{0.2})MnO_3$ consists of short-range correlations (diffuse magnetic scattering) due to the presence of Ho^{3+} and Mn^{2+} at the A site, which coexist with long-range FiM order (magnetic Bragg peaks) down to the lowest measured temperature $T = 1.7$ K. As shown in the inset of Fig. 6, from a linear extrapolation of the average observed Bragg peak intensity of (1, 0, 1) and (0, 2, 0) measured between 45 and 60 K (without contribution from diffuse magnetic scattering), we determined an ordering temperature for the long-range FiM structure of $T_C = 75.6$ (± 1.8) K. The temperature dependence of the magnetic susceptibility shown in Fig. 5a indicates the presence of a small macroscopic FM moment already above T_C which is caused by magnetic short-range correlations (diffuse magnetic scattering observed by neutron diffraction).

In addition to long-range FiM order, also short-range order is observed in $(Ho_{0.8}Mn_{0.2})MnO_3$ at 1.7 K. The neutron diffraction patterns shown in Fig. 2c and with expanded scale in Fig. 7 feature a broad peak of diffuse magnetic intensity (for $10° < 2\theta < 40°$) which gets more pronounced towards low temperature and develops a structure (e.g., near $2\theta = 17°$) indicating some kind of change (or order) of the short-range correlations. A future single crystal neutron diffraction experiment could provide more detailed information. The temperature dependence of neutron intensities observed on the left side ($2\theta = 10°$), on top ($2\theta = 22.5°$) and on the right side ($2\theta = 38.5°$) of the diffuse magnetic intensity peak are plotted in Fig. 8 relative to the paramagnetic intensity at 130 K. The onset of long-range magnetic order is connected to the disappearance of incoherent paramagnetic neutron intensity and results in a decrease of the observed background in a neutron diffraction pattern which according to the square of the magnetic form factor $F(\mathbf{Q})$ is more pronounced for smaller $\mathbf{Q}$ values or smaller 2θ values. At $2\theta = 10°$ and $2\theta = 38.5°$, the expected temperature dependence is observed with a decrease towards 64% and 74%, respectively, at 1.7 K, which is correlated to the growth of the ordered magnetic moments (e.g., accelerated decrease below 20 K). In contrast, at $2\theta = 22.5°$ the observed decrease towards 78% at 1.7 K is too small and indicates that the decrease due to the disappearance of the incoherent paramagnetic neutron intensity is partly compensated by an increase of short-range magnetic correlations.

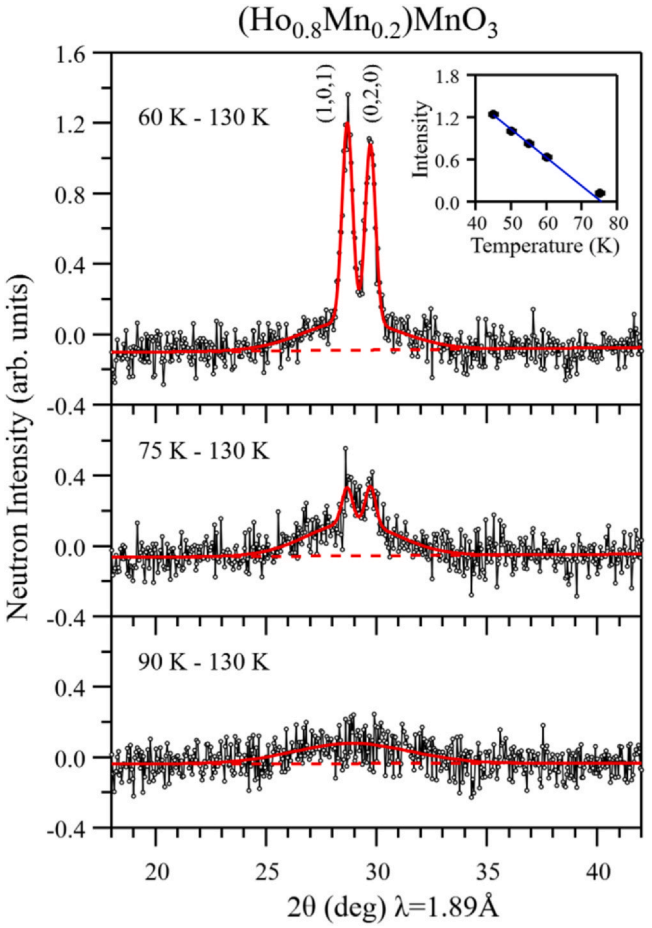

Fig. 6. Magnetic Bragg peaks (1,0,1) and (0,2,0) measured at temperatures near the FiM phase transition at T_C = 76 K. The inset shows a linear extrapolation of the average Bragg peak intensity of (1,0,1) and (0,2,0) measured between 45 and 60 K.

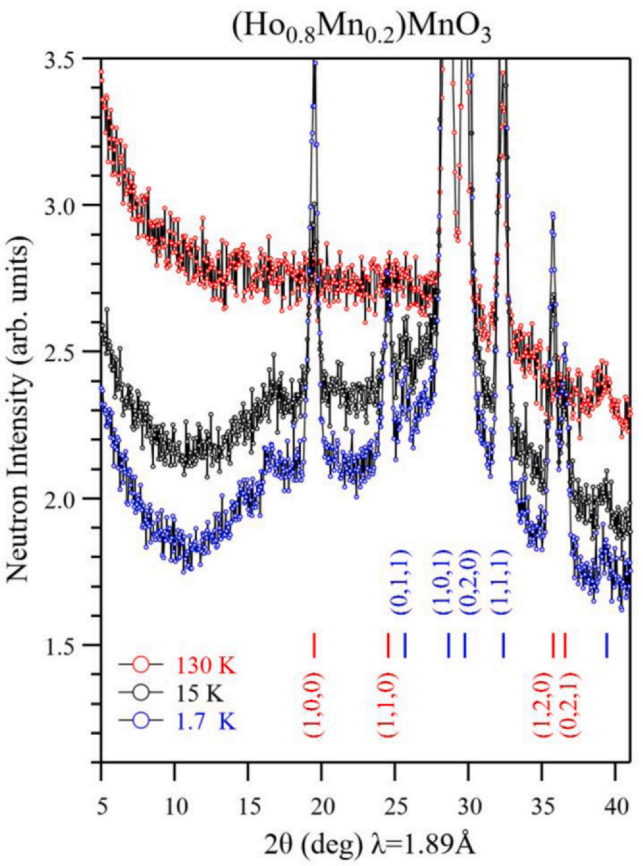

Fig. 7. Low angle part of neutron diffraction patterns measured in the paramagnetic (T = 130 K) and in the magnetically ordered state (T = 15 K and 1.7 K) for $(Ho_{0.8}Mn_{0.2})MnO_3$ shown with an expanded scale.

In the following we compare short-range correlations and long-range FiM ordering found in $(Ho_{0.8}Mn_{0.2})MnO_3$ with the previously studied materials $(Lu_{1-x}Mn_x)MnO_3$ [11,17] and $(Tm_{1-x}Mn_x)MnO_3$ [12,15]. The absence of comparable short-range magnetic ordering in Lu compounds without rare-earth magnetism ($LuMnO_3$, $(Lu_{0.9}Mn_{0.1})MnO_3$ and $(Lu_{0.6}Mn_{0.4})MnO_3$) indicates that mainly rare-earth cations at the A site are responsible. A comparison of Tm compounds (Fig. 9 in Ref. [12]) and Ho compounds (Fig. 8 of this work) reveals that short-range ordering in $(Ho_{0.8}Mn_{0.2})MnO_3$ is stronger than in $(Tm_{0.7}Mn_{0.3})MnO_3$, but weaker than in $(Tm_{0.9}Mn_{0.1})MnO_3$. Thus, in the presence of magnetic rare-earth cations, the strength of short-range magnetic correlations is found to decrease with increasing amount of Mn doping at the A site (x parameter). On the other hand, comparable short-range magnetic ordering is not present in the undoped parent compounds $TmMnO_3$ [15] and $HoMnO_3$ [21].

The FiM Curie temperature T_C (ordering of Mn moments) depends strongly on the x parameter and only weakly on the choice of rare-earth cation. In $(Lu_{0.6}Mn_{0.4})MnO_3$, AFM coupling between the Mn cations at the B and A sites realizes FiM long-range ordering with a macroscopic FM saturation moment of 1.3 μ_B. In both compounds, $(Tm_{0.7}Mn_{0.3})MnO_3$ and $(Ho_{0.8}Mn_{0.2})MnO_3$, the presence of additional rare-earth cations at the A site causes a magnetization reversal behavior at lower temperature. At a first glance, the FiM structures of Tm and Ho compounds seem to be rather similar. But a closer look reveals the difference which is caused by rare-earth exchange interactions that are stronger in Ho^{3+} compared to Tm^{3+}. At the B site (fully occupied by Mn^{3+} and Mn^{4+} cations), the average ordered Mn moment at saturation remains almost unchanged (3.2 μ_B) in $(Lu_{0.6}Mn_{0.4})MnO_3$ and $(Tm_{0.7}Mn_{0.3})MnO_3$ and strongly reduces to (2.3 μ_B) in $(Ho_{0.8}Mn_{0.2})MnO_3$. Furthermore, compared to $(Tm_{1-x}Mn_x)MnO_3$, in $(Ho_{1-x}Mn_x)MnO_3$ the compensation temperature T_{comp} (where the magnetization takes the zero value) is more than twice higher, despite similar values for the FiM ordering temperature T_C. Finally, for $(Ho_{0.8}Mn_{0.2})MnO_3$, in the macroscopic magnetization, the positive maximum near 60 K is reduced to less than half and the negative minimum near 1.7 K is enhanced to more than 3 times.

3.3. Magnetic and dielectric properties of $(Ho_{1-x}Mn_x)MnO_3$

Figs. 9–11 show M versus T and χ versus T curves of $(Ho_{0.8}Mn_{0.2})MnO_3$ and $(Ho_{0.7}Mn_{0.3})MnO_3$. Magnetic transition temperatures were determined from sharp peaks on the 100 Oe FCC $d(\chi T)/dT$ versus T curves as T_C = 76 K for $(Ho_{0.8}Mn_{0.2})MnO_3$ (Fig. S4) and T_C = 102 K for $(Ho_{0.7}Mn_{0.3})MnO_3$ (Fig. S5). Both samples showed qualitatively similar magnetic behavior. They showed sharp increase of FCC magnetic susceptibilities below T_C indicating the development of large uncompensated magnetic moments. At small magnetic fields, FCC magnetic susceptibilities passed through maxima, then decreased, and finally became negative below the compensation temperature (T_{comp}) of about 34–35 K. At larger magnetic fields (such as 2–30 kOe), FCC magnetic susceptibilities exhibited noticeable bending near 35 K. At even larger magnetic fields (such as 50–70 kOe), it looked like FCC magnetic susceptibilities passed through maximum (near 31–33 K) and then bended again near 25–30 K. No noticeable contributions from the $HoMn_3O_6$-type impurity (with a magnetic transition near 70 K [27]) were observed on magnetic properties of $(Ho_{0.7}Mn_{0.3})MnO_3$ probably because of a large dominating FiM moment of $(Ho_{0.7}Mn_{0.3})MnO_3$. Measurements

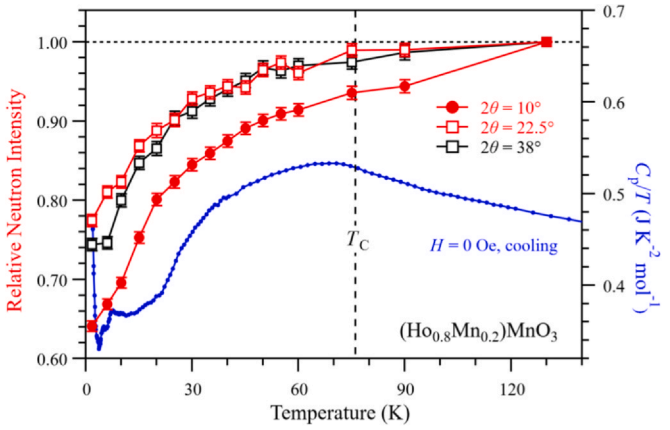

Fig. 8. Temperature dependence of neutron intensities observed at $2\theta = 10°$, 22.5° and 38° (left-hand axis) and specific heat C_p/T (right-hand axis) for $(Ho_{0.8}Mn_{0.2})MnO_3$. Neutron intensities are shown as average of five data points (for $9.9° \le 2\theta \le 10.1°$, $22.4° \le 2\theta \le 22.6°$ and $37.9° \le 2\theta \le 38.1°$) relative to the paramagnetic intensity at 130 K. The vertical dashed line indicates the FiM phase transition at $T_C = 76$ K.

of the ac susceptibilities for different ac fields H_{ac} and different frequencies f are shown in Figs. S6 and S7 for $(Ho_{0.8}Mn_{0.2})MnO_3$. In the temperature dependence of both, the real part (χ') and the imaginary part (χ''), a double peak structure appeared around the

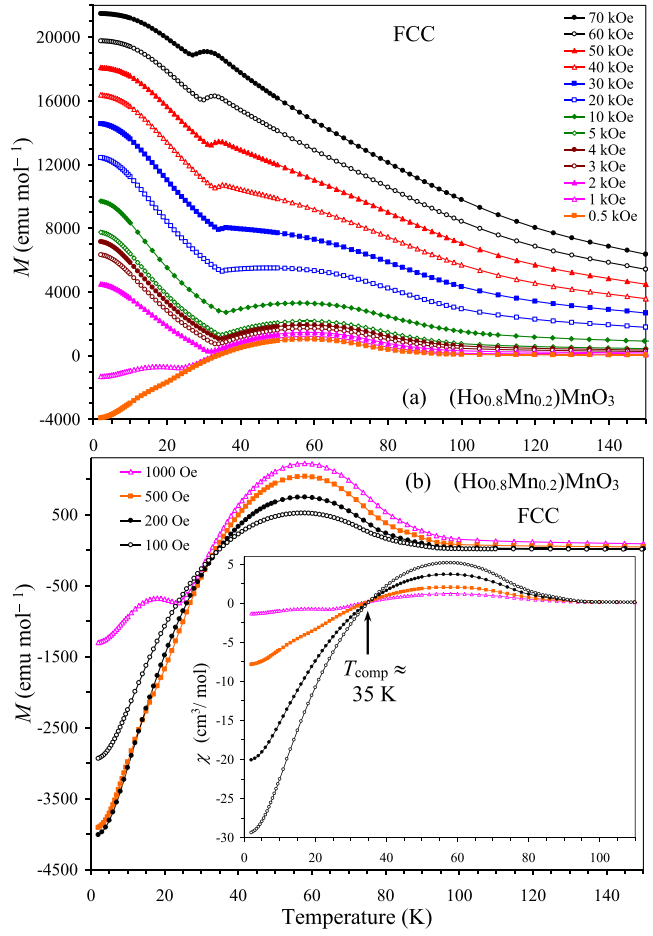

Fig. 9. Temperature dependence of magnetization curves (M versus T) of $(Ho_{0.8}Mn_{0.2})MnO_3$ measured on cooling at different magnetic fields (a) between 70 kOe and 0.5 kOe and (b) between 1 kOe and 0.1 kOe. The inset to (b) gives the χ versus T curves at the same magnetic fields (1, 0.5, 0.2, and 0.1 kOe). FCC: field-cooled on cooling.

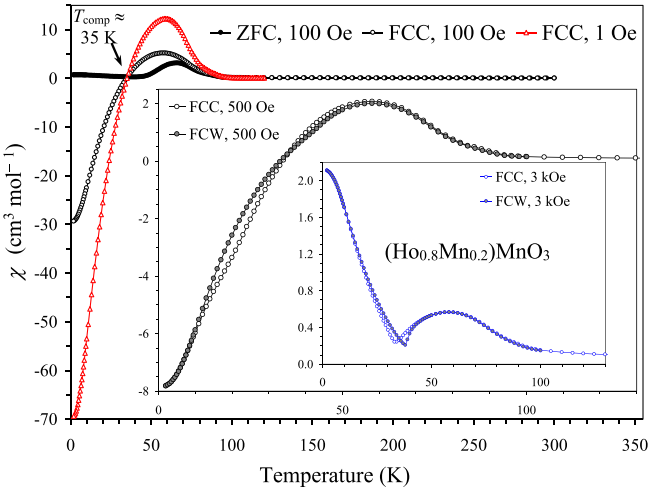

Fig. 10. Temperature dependence of magnetic susceptibility curves (χ versus T) of $(Ho_{0.8}Mn_{0.2})MnO_3$: ZFC at 100 Oe, FCC at 100 Oe, and FCC at 1 Oe. The insets show the FCC and FCW χ versus T curves at 500 Oe and 3 kOe. ZFC: zero-field-cooled, FCC: field-cooled on cooling, FCW: field-cooled on warming.

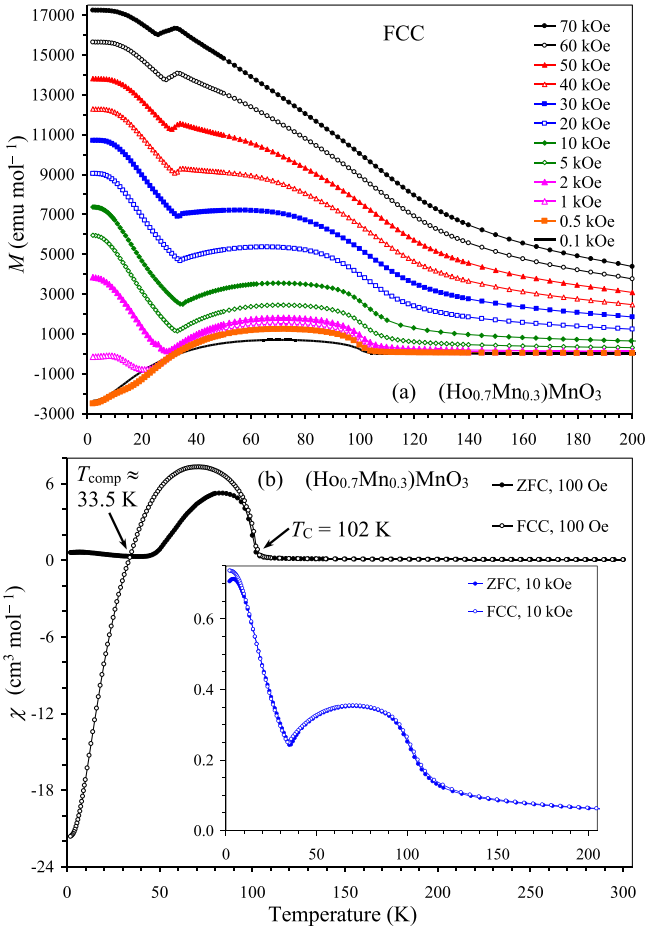

Fig. 11. Temperature dependence of magnetization curves (M versus T) of $(Ho_{0.7}Mn_{0.3})MnO_3$ measured on cooling at different magnetic fields between 70 kOe and 0.1 kOe. (b) Temperature dependence of magnetic susceptibility curves (χ versus T) of $(Ho_{0.7}Mn_{0.3})MnO_3$: ZFC at 100 Oe (black circles) and FCC at 100 Oe (white circles). The inset gives the ZFC and FCC χ versus T curves at 10 kOe.

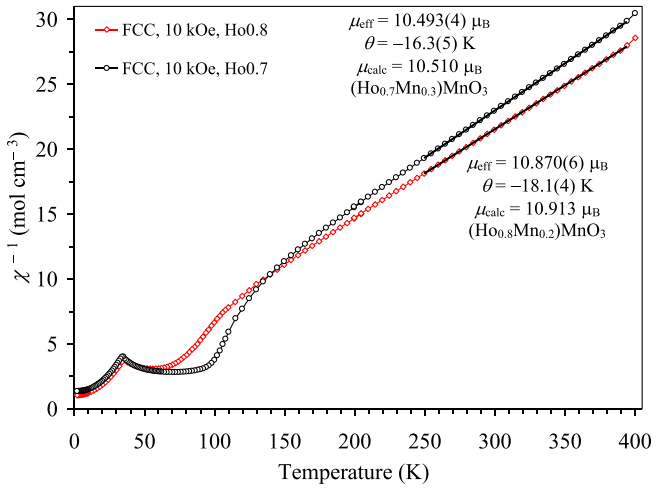

Fig. 12. The FCC χ^{-1} versus T curves at 10 kOe with the Curie-Weiss fits (between 250 and 395 K) for $(Ho_{0.8}Mn_{0.2})MnO_3$ and $(Ho_{0.7}Mn_{0.3})MnO_3$. The obtained fitting parameters and the calculated effective magnetic moments are given on the figure.

FiM ordering temperature T_C = 76 K and a short-range ordering temperature T_{SRO} = 90 K.

The inverse FCC magnetic susceptibilities (measured at 10 kOe) were fitted by the Curie-Weiss equation between 250 and 395 K (Fig. 12)

$$\chi(T) = \mu_{eff}^2 N(3k_B(T-\theta))^{-1} \quad (1)$$

where μ_{eff} is the effective magnetic moment, N is Avogadro's number, k_B is Boltzmann's constant, and θ is the Curie-Weiss temperature. The obtained values are summarized in Fig. 12, where μ_{calc} was calculated using 10.6 μ_B for Ho^{3+} [33]. There was a very good agreement between the observed and calculated effective magnetic moments. The negative Curie-Weiss temperatures show that the strongest exchange interactions are AFM in nature in all compounds. Note that among the magnetic cations Mn2 at the B site and Mn1/Ho at the A site, the nearest neighbors are located on different sites with AFM coupling in the FiM structure.

Isothermal magnetization curves (M versus H) at T = 5 K are given in Fig. 13. They were typical for materials having uncompensated FM

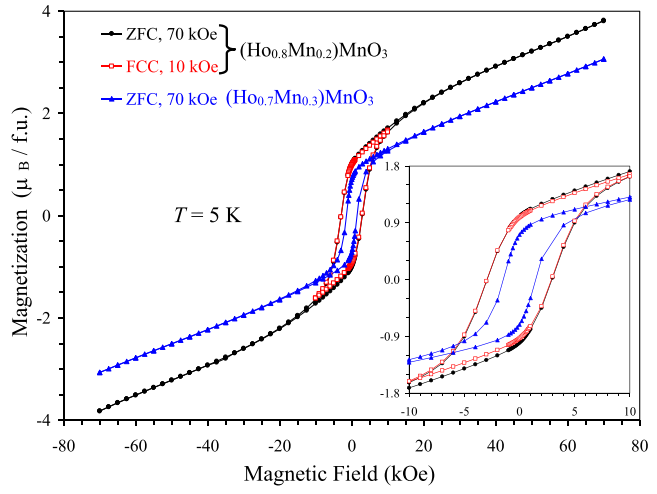

Fig. 13. M versus H curves of $(Ho_{0.8}Mn_{0.2})MnO_3$ and $(Ho_{0.7}Mn_{0.3})MnO_3$ at T = 5 K. f.u.: formula unit. The inset shows details near the origin. In the ZFC procedure, samples were cooled to 5 K from 300 K at zero magnetic field. In the FCC procedure, samples were cooled to 5 K from 300 K under an applied field of 10 kOe.

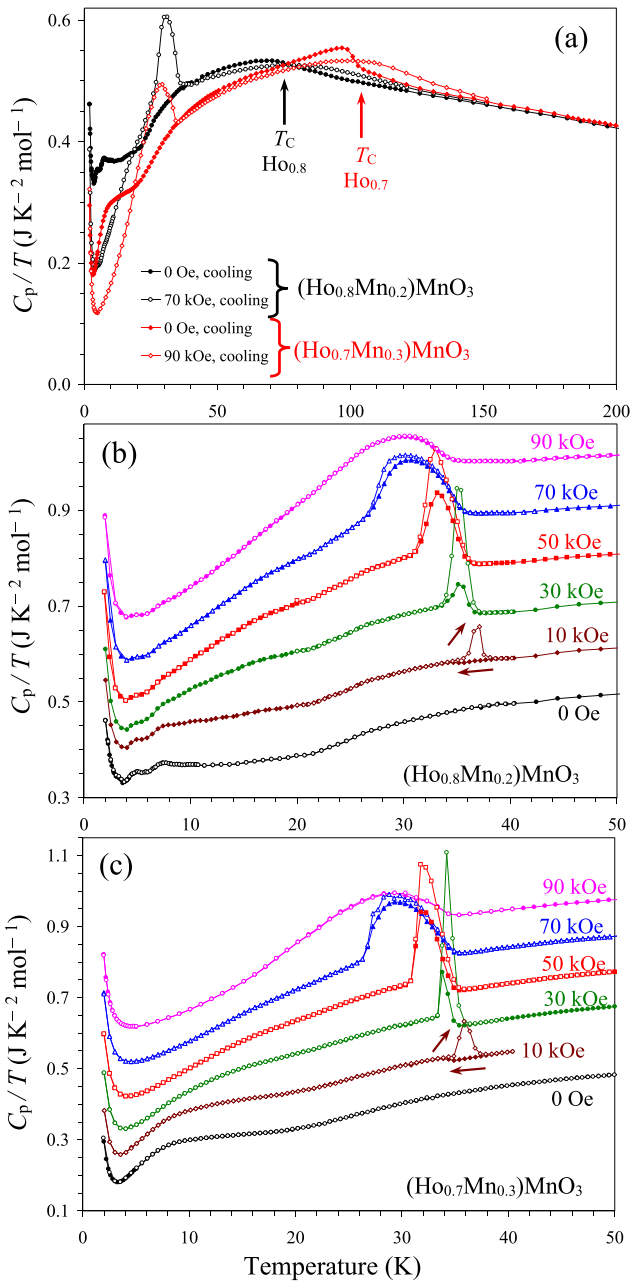

Fig. 14. (a) Specific heat data of $(Ho_{0.8}Mn_{0.2})MnO_3$ and $(Ho_{0.7}Mn_{0.3})MnO_3$, plotted as C_p/T versus T. Curves measured on cooling at H = 0 Oe and 70 (or 90) kOe are shown. (b) C_p/T versus T curves of $(Ho_{0.8}Mn_{0.2})MnO_3$ measured on cooling (filled symbols) and heating (empty symbols) at different magnetic fields of 0, 10, 30, 50, 70, and 90 kOe. (c) C_p/T versus T curves of $(Ho_{0.7}Mn_{0.3})MnO_3$ measured on cooling (filled symbols) and heating (empty symbols) at different magnetic fields of 0, 10, 30, 50, 70, and 90 kOe. On panels (b) and (c) the curves are shifted by 0.1 J K^{-2} mol^{-1} from each other (except the zero-field data) for the clarity.

moments. At T = 5 K and H = 70 kOe, magnetization reached 3.82 μ_B/f.u. for $(Ho_{0.8}Mn_{0.2})MnO_3$ and 3.07 μ_B/f.u. for $(Ho_{0.7}Mn_{0.3})MnO_3$. The remnant magnetization at T = 5 K was about 1.00 μ_B/f.u. for $(Ho_{0.8}Mn_{0.2})MnO_3$ and 0.71 μ_B/f.u. for $(Ho_{0.7}Mn_{0.3})MnO_3$. The magnetization extrapolated between 40 and 70 kOe to zero field was 1.74 μ_B/f.u. for $(Ho_{0.8}Mn_{0.2})MnO_3$ and 1.12 μ_B/f.u. for $(Ho_{0.7}Mn_{0.3})MnO_3$. The coercive field at T = 5 K was about 3 kOe for $(Ho_{0.8}Mn_{0.2})MnO_3$ and 1.5 kOe for $(Ho_{0.7}Mn_{0.3})MnO_3$.

Specific heat data for $(Ho_{0.8}Mn_{0.2})MnO_3$ and $(Ho_{0.7}Mn_{0.3})MnO_3$ are presented in Fig. 14. An anomaly was observed at T_C of $(Ho_{0.7}Mn_{0.3})MnO_3$ at H = 0 Oe confirming a long-range magnetic

ordering. But an anomaly at T_C for $(Ho_{0.8}Mn_{0.2})MnO_3$ was noticeably smeared. The C_p/T values at $H = 0$ Oe demonstrated an additional bump below about 25 K originating probably from the Ho^{3+} contribution. No hysteresis was observed on cooling and heating at $H = 0$ Oe. We note that the 'wavy' behavior of the C_p/T values at $H = 0$ Oe for $(Ho_{0.8}Mn_{0.2})MnO_3$ between 3 and 8 K was confirmed on samples from different synthesis batches; therefore, such behavior should be intrinsic. At magnetic fields of 10–70 kOe, clear hysteresis was observed on cooling and heating with clear peaks on the heating curves near 35 K. At $H = 90$ kOe, the hysteresis almost disappeared again, but very broad anomalies remained in comparison with the $H = 0$ Oe data. The widths of the peaks became wider with the increase of the applied magnetic field. These results suggest the presence of first-order field-induced transitions in both compounds. No dielectric anomalies were observed in $(Ho_{0.8}Mn_{0.2})MnO_3$ at $H = 0$–90 kOe suggesting that neither a FiM transition at T_C nor a field-induced transition near 35 K produce spin-induced ferroelectricity (Figs. S8 and S9).

4. Conclusion

In this work, we extended the family of Mn-self doped perovskite solid solutions $(R_{1-x}Mn_x)MnO_3$ to R = Ho. We found that the solubility limit (x) shrinks with the increase of the size of rare-earth cations. We investigated magnetic and dielectric properties of $(Ho_{1-x}Mn_x)MnO_3$ with $x = 0.2$ and 0.3 and determined the magnetic structure of $(Ho_{0.8}Mn_{0.2})MnO_3$ and its evolution with temperature. Pronounced magnetization reversal effects and field-induced first-order transitions are realized in $(Ho_{1-x}Mn_x)MnO_3$ with $x = 0.2$ and 0.3.

CRediT authorship contribution statement

Andreas Dönni: Investigation, Formal analysis, Writing - original draft. **Vladimir Y. Pomjakushin**: Investigation. **Lei Zhang**: Investigation. **Kazunari Yamaura**: Funding acquisition. **Alexei A. Belik**: Conceptualization, Investigation, Formal analysis, Writing - original draft, Writing - review & editing.

Declaration of Competing Interest

The authors declare that they have no known competing financial interests or personal relationships that could have appeared to influence the work reported in this paper.

Acknowledgements

This work is partially based on experiments performed on HRPT diffractometer (Proposal No. 20180113) at the Swiss Spallation Neutron Source SINQ, Paul Scherrer Institute, Switzerland. This work was partly supported by JSPS KAKENHI Grant Number JP20H05276, a research grant (40-37) from Nippon Sheet Glass Foundation for Materials Science and Engineering, and Innovative Science and Technology Initiative for Security (Grant Number JPJ004596) from Acquisition, Technology, and Logistics Agency (ATLA), Japan.

Appendix A. Supporting information

Supplementary data associated with this article can be found in the online version at doi:10.1016/j.jallcom.2020.158230.

References

[1] E. Bousquet, A. Cano, Non-collinear magnetism in multiferroic perovskites, J. Phys. Condens. Matter 28 (2016) 123001, , https://doi.org/10.1088/0953-8984/28/12/123001.
[2] A.V. Kimel, A. Kirilyuk, A. Tsvetkov, R.V. Pisarev, Th. Rasing, Laser-induced ultrafast spin reorientation in the antiferromagnet $TmFeO_3$, Nat. (Lond.) 429 (2004) 850–853, https://doi.org/10.1038/nature02659.
[3] K. Yoshii, Spin rotation, glassy state, and magnetization switching in $RCrO_3$ (R = $La_{1-x}Pr_x$, Gd, and Tm): reinvestigation of magnetization reversal, J. Appl. Phys. 126 (2019) 123904, , https://doi.org/10.1063/1.5116205.
[4] O.V. Billoni, F. Pomiro, S.A. Cannas, C. Martin, A. Maignan, R.E. Carbonio, Magnetization reversal in mixed ferrite-chromite perovskites with non magnetic cation on the A-site, J. Phys. Condens. Matter 28 (2016) 476003, , https://doi.org/10.1088/0953-8984/28/47/476003.
[5] T. Kimura, T. Goto, H. Shintani, K. Ishizaka, T. Arima, Y. Tokura, Magnetic control of ferroelectric polarization, Nat. (Lond.) 426 (2003) 55–58, https://doi.org/10.1038/nature02018.
[6] A.M. Oleś, Fingerprints of spin-orbital entanglement in transition metal oxides, J. Phys. Condens. Matter 24 (2012) 313201, , https://doi.org/10.1088/0953-8984/24/31/313201.
[7] J. Hemberger, F. Schrettle, A. Pimenov, P. Lunkenheimer, V. Yu. Ivanov, A.A. Mukhin, A.M. Balbashov, A. Loidl, Multiferroic phases of $Eu_{1-x}Y_xMnO_3$, Phys. Rev. B 75 (2007) 035118, , https://doi.org/10.1103/PhysRevB.75.035118.
[8] Y. Yamasaki, H. Sagayama, N. Abe, T. Arima, K. Sasai, M. Matsuura, K. Hirota, D. Okuyama, Y. Noda, Y. Tokura, Cycloidal spin order in the a-axis polarized ferroelectric phase of orthorhombic perovskite manganite, Phys. Rev. Lett. 101 (2008) 097204, , https://doi.org/10.1103/PhysRevLett.101.097204.
[9] J.P. Bolletta, F. Pomiro, R.D. Sánchez, V. Pomjakushin, G. Aurelio, A. Maignan, C. Martin, R.E. Carbonio, Spin reorientation and metamagnetic transitions in $RFe_{0.5}Cr_{0.5}O_3$ perovskites (R = Tb, Dy, Ho, Er), Phys. Rev. B 98 (2018) 134417, , https://doi.org/10.1103/PhysRevB.98.134417.
[10] L. Zhang, D. Gerlach, A. Dönni, T. Chikyow, Y. Katsuya, M. Tanaka, S. Ueda, K. Yamaura, A.A. Belik, Mn self-doping of orthorhombic $RMnO_3$ perovskites: $(R_{0.667}Mn_{0.333})MnO_3$ with R = Er-Lu, Inorg. Chem. 57 (2018) 2773–2781, https://doi.org/10.1021/acs.inorgchem.7b03188.
[11] L. Zhang, A. Dönni, V.Y. Pomjakushin, K. Yamaura, A.A. Belik, Crystal and magnetic structures and properties of $(Lu_{1-x}Mn_x)MnO_3$ solid solutions, Inorg. Chem. 57 (2018) 14073–14085, https://doi.org/10.1021/acs.inorgchem.8b01470.
[12] A. Dönni, V.Y. Pomjakushin, L. Zhang, K. Yamaura, A.A. Belik, Origin of negative magnetization phenomena in $(Tm_{1-x}Mn_x)MnO_3$: a neutron diffraction study, Phys. Rev. B 101 (2020) 054442, , https://doi.org/10.1103/PhysRevB.101.054442.
[13] M. Tachibana, T. Shimoyama, H. Kawaji, T. Atake, E. Takayama-Muromachi, Jahn-Teller distortion and magnetic transitions in perovskite $RMnO_3$ (R = Ho, Er, Tm, Yb, and Lu), Phys. Rev. B 75 (2007) 144425, , https://doi.org/10.1103/PhysRevB.75.144425.
[14] F. Ye, B. Lorenz, Q. Huang, Y.Q. Wang, Y.Y. Sun, C.W. Chu, J.A. Fernandez-Baca, Pengcheng Dai, H.A. Mook, Incommensurate magnetic structure in the orthorhombic perovskite $ErMnO_3$, Phys. Rev. B 76 (2007) 060402, , https://doi.org/10.1103/PhysRevB.76.060402.
[15] V.Y. Pomjakushin, M. Kenzelmann, A. Dönni, A.B. Harris, T. Nakajima, S. Mitsuda, M. Tachibana, L. Keller, J. Mesot, H. Kitazawa, E. Takayama-Muromachi, Evidence for large electric polarization from collinear magnetism in $TmMnO_3$, New J. Phys. 11 (2009) 043019, , https://doi.org/10.1088/1367-2630/11/4/043019.
[16] Y.H. Huang, H. Fjellvåg, M. Karppinen, B.C. Hauback, H. Yamauchi, J.B. Goodenough, Crystal and magnetic structure of the orthorhombic perovskite $YbMnO_3$, Chem. Mater. 18 (2006) 2130–2134, https://doi.org/10.1021/cm052758t.
[17] S. Mukherjee, A. Dönni, T. Nakajima, S. Mitsuda, M. Tachibana, H. Kitazawa, V. Pomjakushin, L. Keller, C. Niedermayer, A. Scaramucci, M. Kenzelmann, E-type noncollinear magnetic ordering in multiferroic o-$LuMnO_3$, Phys. Rev. B 95 (2017) 104412, , https://doi.org/10.1103/PhysRevB.95.104412.
[18] C.N.R. Rao, A.K. Cheetham, R. Mahesh, Giant magnetoresistance and related properties of rare-earth manganates and other oxide systems, Chem. Mater. 8 (1996) 2421–2432, https://doi.org/10.1021/cm960201v.
[19] J.M.D. Coey, M. Viret, S. von Molnar, Mixed-valence manganites, Adv. Phys. 58 (2009) 571–697, https://doi.org/10.1080/00018730903363184.
[20] A.P. Ramirez, Colossal magnetoresistance, J. Phys. Condens. Matter 9 (1997) 8171–8199, https://doi.org/10.1088/0953-8984/9/39/005.
[21] A. Munoz, M.T. Casais, J.A. Alonso, M.J. Martinez-Lope, J.L. Martinez, M.T. Fernandez-Diaz, Complex magnetism and magnetic structures of the metastable $HoMnO_3$ perovskite, Inorg. Chem. 40 (2001) 1020–1028, https://doi.org/10.1021/ic0011009.
[22] B. Lorenz, Y.Q. Wang, C.W. Chu, Ferroelectricity in perovskite $HoMnO_3$ and $YMnO_3$, Phys. Rev. B 76 (2007) 104405, , https://doi.org/10.1103/PhysRevB.76.104405.
[23] N. Lee, Y.J. Choi, M. Ramazanoglu, W. Ratcliff, V. Kiryukhin, S.W. Cheong, Mechanism of exchange striction of ferroelectricity in multiferroic orthorhombic $HoMnO_3$ single crystals, Phys. Rev. B 84 (2011) 020101, , https://doi.org/10.1103/PhysRevB.84.020101.
[24] H.W. Brinks, R. Rodriguez-Carvajal, H. Fjellvåg, A. Kjekshus, B.C. Hauback, Crystal and magnetic structure of orthorhombic $HoMnO_3$, Phys. Rev. B 63 (2001) 094411, , https://doi.org/10.1103/PhysRevB.63.094411.
[25] P. Fischer, G. Frey, M. Koch, M. Könnecke, V. Pomjakushin, J. Schefer, R. Thut, N. Schlumpf, R. Bürge, U. Greuter, S. Bondt, E. Berruyer, High-resolution powder diffractometer HRPT for thermal neutrons at SINQ, Phys. B 276 (2000) 146–147, https://doi.org/10.1016/S0921-4526(99)01399-X.
[26] J. Rodriguez-Carvajal, Recent advances in magnetic structure determination by neutron powder diffraction, Phys. B 192 (1993) 55–69, https://doi.org/10.1016/0921-4526(93)90108-I.

[27] L. Zhang, Y. Matsushita, K. Yamaura, A.A. Belik, Five-fold ordering in high-pressure perovskites RMn_3O_6 (R = Gd-Tm and Y), Inorg. Chem. 56 (2017) 5210–5218, https://doi.org/10.1021/acs.inorgchem.7b00347.
[28] R. Rodriguez-Carvajal, M.T. Fernandez-Diaz, J.L. Martinez, Neutron diffraction study on structural and magnetic properties of La_2NiO_4, J. Phys. Condens. Matter 3 (1991) 3215–3234, https://doi.org/10.1088/0953-8984/3/19/002.
[29] P.W. Stephens, Phenomenological model of anisotropic peak broadening in powder diffraction, J. Appl. Cryst. 32 (1999) 281–289, https://doi.org/10.1107/S0021889898006001.
[30] N.E. Brese, M. O'Keeffe, Bond-valence parameters for solids, Acta Crystallogr. B 47 (1991) 192–197, https://doi.org/10.1107/S0108768190011041.
[31] D.B. Litvin, in: Magnetic Group Tables, International Union of Crystallography, (2013), ⟨https://www.iucr.org/publ/978-0-9553602-2-0⟩.
[32] K. Momma, F. Izumi, VESTA 3 for three-dimensional visualization of crystal, volumetric and morphology data, J. Appl. Crystallogr. 44 (2011) 1272–1276, https://doi.org/10.1107/S0021889811038970.
[33] C. Kittel, Introduction to Solid State Physics, 8th ed., John Wiley and Sons, Inc, New York, 2005 (ISBN: 978-0-471-41526-8).